



## RESEARCH ARTICLE

10.1002/2014GB004913

## Key Points:

- NCP and export decouple on scales below 5 km yet balance on mesoscales
- Biogeochemical fluxes vary more strongly than coincident physical parameters
- Higher trophic level biogeochemical parameters were more spatially variable

## Supporting Information:

- Readme
- Figure S1
- Figure S2
- Figure S3
- Figure S4
- Figure S5
- Figure S6
- Figure S7
- Figure S8
- Figure S9
- Table S1

## Correspondence to:

M. L. Estapa,  
mestapa@skidmore.edu

## Citation:

Estapa, M. L., D. A. Siegel, K. O. Buesseler, R. H. R. Stanley, M. W. Lomas, and N. B. Nelson (2015), Decoupling of net community and export production on submesoscales in the Sargasso Sea, *Global Biogeochem. Cycles*, 29, 1266–1282, doi:10.1002/2014GB004913.

Received 6 JUN 2014

Accepted 13 JUL 2015

Accepted article online 18 JUL 2015

Published online 31 AUG 2015

## Decoupling of net community and export production on submesoscales in the Sargasso Sea

M. L. Estapa<sup>1,2</sup>, D. A. Siegel<sup>3</sup>, K. O. Buesseler<sup>1</sup>, R. H. R. Stanley<sup>1,4</sup>, M. W. Lomas<sup>5,6</sup>, and N. B. Nelson<sup>3</sup>

<sup>1</sup>Department of Marine Chemistry and Geochemistry, Woods Hole Oceanographic Institution, Woods Hole, Massachusetts, USA, <sup>2</sup>Now at Department of Geosciences, Skidmore College, Saratoga Springs, New York, USA, <sup>3</sup>Earth Research Institute and Department of Geography, University of California, Santa Barbara, California, USA, <sup>4</sup>Now at Department of Chemistry, Wellesley College, Wellesley, Massachusetts, USA, <sup>5</sup>Bermuda Institute of Ocean Sciences, St. Georges, Bermuda, <sup>6</sup>Now at Bigelow Laboratory for Ocean Sciences, East Boothbay, Maine, USA

**Abstract** Determinations of the net community production (NCP) in the upper ocean and the particle export production (EP) should balance over long time and large spatial scales. However, recent modeling studies suggest that a horizontal decoupling of flux-regulating processes on submesoscales ( $\leq 10$  km) could lead to imbalances between individual determinations of NCP and EP. Here we sampled mixed-layer biogeochemical parameters and proxies for NCP and EP during 10, high-spatial resolution ( $\sim 2$  km) surface transects across strong physical gradients in the Sargasso Sea. We observed strong biogeochemical and carbon flux variability in nearly all transects. Spatial coherence among measured biogeochemical parameters within transects was common but rarely did the same parameters covary consistently across transects. Spatial variability was greater in parameters associated with higher trophic levels, such as chlorophyll in  $>5.0$   $\mu\text{m}$  particles, and variability in EP exceeded that of NCP in nearly all cases. Within sampling transects, coincident EP and NCP determinations were uncorrelated. However, when averaged over each transect (30 to 40 km in length), we found NCP and EP to be significantly and positively correlated ( $R = 0.72$ ,  $p = 0.04$ ). Transect-averaged EP determinations were slightly smaller than similar NCP values (Type-II regression slope of 0.93, standard deviation = 0.32) but not significantly different from a 1:1 relationship. The results show the importance of appropriate sampling scales when deriving carbon flux budgets from upper ocean observations.

### 1. Introduction

The delivery of organic carbon from the surface, oligotrophic ocean to deep waters below the thermocline, termed “the biological pump”, plays a key role in the regulation of global climate [Volk and Hoffert, 1985; Falkowski *et al.*, 1998]. Export production (EP) is the biologically fixed carbon that escapes remineralization in the upper ocean through gravitational settling through some defined depth, active transport by vertically migrating zooplankton, or by net physical transport of organic carbon to below the main thermocline. Net community production, on the other hand, is typically quantified by tracking rates of change in stocks of photosynthetic precursors (i.e., dissolved inorganic carbon, nutrients plus an assumed carbon-to-nutrient ratio) or byproducts (i.e., dissolved oxygen and its isotopes). By definition, carbon export should balance net community production when integrated over sufficiently large spatiotemporal scales [Brix *et al.*, 2006]. However, there are few simultaneous measurements of both EP and net community production (NCP); and as we discuss below, those that do exist typically do not agree over observational scales, suggesting either that the two fluxes are decoupled or that methodological biases exist. Several discussions in the literature suggest that biological rates and fluxes (e.g., production and respiration, net autotrophy, and plankton community structure) are spatiotemporally variable over short scales [e.g., Richerson *et al.*, 1970; Siegel *et al.*, 2001; Karl *et al.*, 2003; d’Ovidio *et al.*, 2010], and measured imbalances further support the idea that they are decoupled in the surface, oligotrophic ocean [e.g., Karl *et al.*, 2003]. In this study, we show observations of NCP and EP that are in agreement when measured simultaneously at high resolution and averaged up to appropriate spatial scales.

Recent observational studies, utilizing different combinations of NCP and export measurement methods, illustrate the vertical decoupling of the processes driving these fluxes in the upper part of the euphotic zone. For example, Alkire *et al.* [2012] utilized sensors on autonomous floats and gliders to track budgets of nitrate and  $\text{O}_2$  and estimate NCP in the mixed layer during the North Atlantic spring bloom. Even after

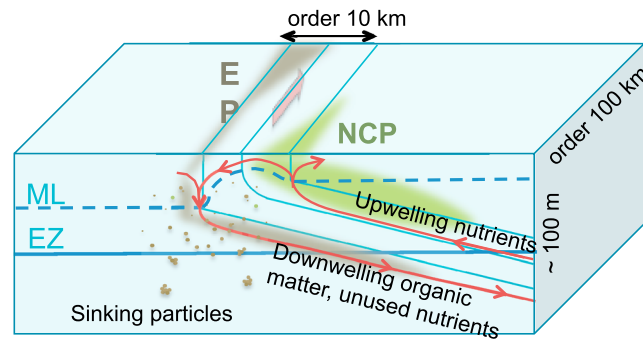


**Figure 1.** Schematic representation of a submesoscale “hot spot” in nutrient-depleted waters and its evolution along a spatially varying, physical front (adapted from Figure 2 in Lévy *et al.* [2012]). “EP” = Export production, “NCP” = Net community production, “ML” = mixed layer, and “EZ” = euphotic zone. Thin blue lines show shoaling isopycnals at the front, the thick blue dashed line shows the ML, and the thick solid blue line shows the EZ.

subeuphotic zone export with sediment traps. After accounting for DOC production, mixed-layer NCP exceeded measured POC export, suggesting strong submixed-layer remineralization [Martin *et al.*, 2013].

Recent observational and modeling studies suggest that NCP and export can also be horizontally decoupled on submesoscales, defined here as scales smaller than 10 km. Calil and Richards [2010] identified submesoscale filaments of high-resolution satellite chlorophyll-*a* encircling a mesoscale eddy, and these filaments aligned well with bands of converging streamlines modeled from sea surface altimetry. Guidi *et al.* [2012] conducted a high-resolution spatial survey of a boundary between two eddies. They found intensified phytoplankton production and export associated with predicted bands of submesoscale divergence, although they did not measure NCP. Moreover, other studies have shown enhanced, mixed-layer NCP variations on submesoscales using underway  $O_2/Ar$  saturation measurements [Stanley *et al.*, 2010; R. H. R. Stanley and D. McGillicuddy, Submesoscale hotspots of productivity and respiration: Insights from high-resolution oxygen and fluorescence sections, in review at *Deep Sea Research I*, 2015], even in the presence of a likely oxygen debt from low- $O_2$  water mixed upward from greater depths (R. H. R. Stanley and D. McGillicuddy, manuscript in review, 2015).

Using a model framework, Lévy *et al.* [2012] discuss physical mechanisms by which production and export can be enhanced along submesoscale fronts. Enhanced vertical velocities at these fronts can inject nutrients into the euphotic zone, increasing production and ecosystem-modulated particle export, while also leading to subduction of DOC and suspended POC [Lévy *et al.*, 2012]. Resplandy *et al.* [2012] modeled  $^{234}Th$  export with a submesoscale-resolving, dynamical-biogeochemical model and similarly predicted strong, horizontal gradients in particle export at these scales. Importantly, these authors hypothesized that these gradients were able to persist over  $^{234}Th$  decay time scales without dissipating because submesoscale structures present were barriers to horizontal mixing. Harrison *et al.* [2013] modeled larval transport in a coastal upwelling system using a submesoscale-resolving model and predicted high concentrations of weeks old to months old larvae within eddy-associated filaments and frontal structures only a few kilometers across. Similarly, during the Southern Ocean Iron Release Experiment iron fertilization experiment, high-strain rates led to development of a narrow (~4 km wide), productive filament that persisted for 55 days [Abraham *et al.*, 2000].

The horizontal decoupling of EP and NCP in the vicinity of submesoscale fronts is not unexpected for nutrient-depleted, oligotrophic waters (Figure 1; adapted from Lévy *et al.* [2012]). Ageostrophic circulation across a submesoscale (SMS) front will drive upwelling of nutrients on the warm (light) side of the front which should elevate rates of NCP while on the cool side of the front downwelling, and convergence of surface waters may enhance particle aggregation processes leading to elevated rates of export (Figure 1). In this idealization, areas of high NCP and high export will be separated vertically, horizontally, and temporally across an SMS front, which presents a barrier to mixing. Submesoscale features extract the energy needed for their formation from larger scales and are typically found on the high-velocity regions

accounting for net dissolved organic carbon (DOC) production in the mixed layer, the authors found a mismatch between their NCP-derived estimate of particulate organic carbon (POC) export from the mixed layer and the POC export measured below the euphotic zone with sediment traps. Reconciliation of the difference required either intense upper ocean remineralization or horizontal decoupling of NCP and export [Alkire *et al.*, 2012]. Further, during the LOHAFEX iron fertilization study, Martin *et al.* [2013] measured mixed-layer NCP using underway  $O_2/Ar$  saturation measurements, POC export in the upper euphotic zone below the mixed layer with  $^{234}Th$  deficit measurements, and

surrounding mesoscale eddies [e.g., *d'Ovidio et al.*, 2004; *Calil and Richards*, 2010; *Harrison and Glatzmaier*, 2010]. These SMS features have been observed to persist for many weeks and evolve physically and biologically on time scales of days to a few weeks [e.g., *Lévy et al.*, 2012; *Samelson*, 2013]. Thus, observational “snapshots” of NCP and EP crossing identified SMS features might easily fail to reflect a balance between these fluxes. However, when averaged over larger spatial scales and many SMS fronts, such as the entire domain depicted in Figure 1, measurements of NCP and EP in principle will correspond to each other.

In the present study, we used satellite observations and satellite-derived calculations of surface water parcel dispersal to guide ship-based sampling of NCP, EP, and biogeochemical properties across small-scale ( $\leq 40$  km) frontal features from two meridional transects across the Sargasso Sea. Our observations, presented in the remainder of this paper, represent the first (to our knowledge) coupled NCP and EP measurements made that directly target SMS features. The data show that NCP and EP have different scales of variability and are clearly decoupled on submesoscales ( $\leq 10$  km) but are broadly consistent over larger scales consistent with our cartoon depiction illustrating the spatial imbalance between NCP and EP (Figure 1).

## 2. Methods

### 2.1. Sampling Plan

The broader cruise track was a meridional transect across the western Sargasso Sea during both surveys, which limited the high-resolution sampling presented in this study to frontal features located near longitude  $64^{\circ}10'W$  (excepting a jog to the west in 2011 to avoid Hurricane Ophelia). Candidate features throughout the western Sargasso Sea were identified through analysis of available near-real-time satellite chlorophyll, sea surface temperature (SST), and sea surface height (SSH) imagery, as well as computations of finite-time Lyapunov exponents (FTLE) from near-real-time satellite altimetry-determined geostrophic flow fields (details below). Before sailing, the cruise was planned around the predicted locations and intensities of these features, and updates were communicated to the ship at sea several times each day. In 2012, along-track sea surface temperature and salinity were additionally used to center sampling transects across the strongest physical gradients.

Finite-time Lyapunov exponents measure the rate of separation of adjacent surface water parcels as a function of time, and these metrics are proving increasingly useful in interpreting interdisciplinary oceanographic observations [*d'Ovidio et al.*, 2004, 2010; *Shadden et al.*, 2009; *Calil and Richards*, 2010; *Nencioli et al.*, 2011; *Harrison et al.*, 2013; *Samelson*, 2013]. Elevated FTLE values indicate locations where surface water parcels are diverging from or converging with each other and are often distributed in “ridges” that are referred to as Lagrangian Coherent Structures (LCS) [*d'Ovidio et al.*, 2004; *Samelson*, 2013]. We hypothesized that areas characterized by the presence of attracting or repelling FTLE ridges would have enhanced SMS variability and thereby increased biogeochemical activity.

Values of FTLEs were determined by numerically advecting a dense cloud of surface water parcels ( $\sim 2.8$  km spatial resolution) forward in time using geostrophic velocities calculated from merged satellite altimetry observations (<http://www.avisioceanobs.com/duacs/>) and evaluating the mean rate of separation between a given particle and its neighbors over a 21 day time interval. This provided the locations of “repelling” (diverging) SMS features. FTLEs were also calculated by advecting particles backward in time, providing the locations of “attracting” (converging) SMS features. Repelling and attracting FTLEs were calculated using both near-real-time and postcruise merged satellite altimetry fields, and near-real-time repelling FTLEs were calculated assuming a frozen field hypothesis. Since the FTLEs were calculated using  $1/4^{\circ}$  mapped geostrophic velocity fields modeled from satellite altimeter ground tracks, a point-to-point comparison of their locations with the 2 km resolution field observations (see below) is not sensible.

### 2.2. Submesoscale Transect Sampling

A total of 10 transects across areas with predicted, high-FTLE ridges were surveyed during the two Bermuda Atlantic Time-series Study (BATS) validation transect cruises in the Sargasso Sea during autumn 2011 and 2012 (Figure 2 and Table 1). In addition to proxies for NCP and export, most transects included measurements of a suite of biogeochemical, phytoplankton and optical properties, as well as radiometric

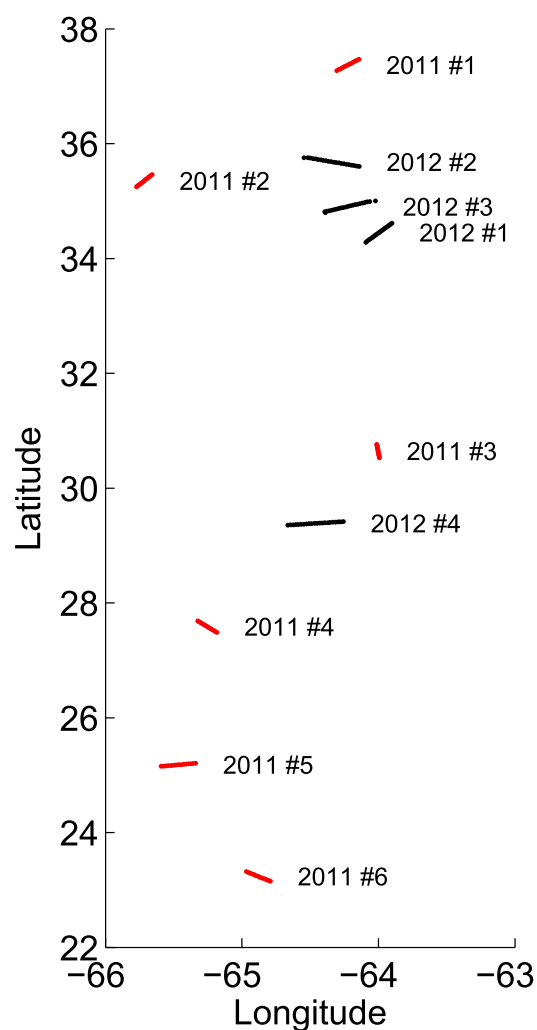


**Figure 2.** Map showing locations of surface transects across strong submesoscale physical gradients (see Table 1 for details). Red lines show 2011 transect paths, black lines show 2012 transects.

observations during daytime sampling. Surface, along-track samples were collected during 30 km or 40 km long (for the 2011 and 2012 surveys, respectively) transects oriented roughly orthogonally to constant SSH surfaces and predicted ridges of high-FTLE values. The selected transects corresponded to fronts identified from the few available satellite images (supporting information Figure S1). All transects were bracketed by a pair of conductivity-temperature-depth (CTD) casts to 300 m. Discrete, underway samples were spaced ~2 km apart along each transect. A high-flow, clean seawater intake, extended below the ship's moon pool and driven by a clean, compressed air-powered diaphragm pump, was used for all discrete surface samples. About 5 min were required to collect water for all analytes, leading to a spatial uncertainty of about 0.6 km at the steaming speed of 4 knots. Including wire time at the endpoints, each high-resolution transect required about 8–10 h to sample completely. Ship time constraints did not allow for collection of pumped samples for particulate carbon to <sup>234</sup>Th ratios (C:<sup>234</sup>Th).

Endpoint CTD casts included bottle samples for <sup>234</sup>Th deficits, discrete O<sub>2</sub>/Ar samples, high-performance liquid chromatography (HPLC) pigments, particulate organic carbon and nitrogen (POC/PON), and flow cytometric cell counts. Mixed-layer biological oxygen saturation was

measured continuously during transects across the SMS features. The long-track discrete sample suite was the same as for CTD bottles, with the addition of size-fractionated fluorometric chlorophyll and transparent exopolymer particles (TEP). Each analytical method is detailed below.

**2.3. Computations of Reference Depths**

Mixed-layer depths were computed from density profiles using a difference threshold of  $\sigma_\theta = +0.15 \text{ kg m}^{-3}$  above the surface density. Most transects were sampled at night; therefore, we do not have simultaneous optical estimates of the euphotic zone depth. However, an in situ chlorophyll fluorometer was present on every CTD cast, and this was used to locate the lower boundary of the layer containing most autotrophic biomass, which we term the "particle production zone" (PPZ). We defined the PPZ depth specifically as the depth beneath the chlorophyll maximum where fluorescence drops to less than 10% of its maximum value (see Owens et al. [2015] for detailed discussion of methodology and Marra et al. [2014] for direct comparisons to radiometry and measurements of the compensation depth).

**2.4. <sup>234</sup>Th Deficit and Carbon Export**

Samples for total (dissolved + particulate) <sup>234</sup>Th were collected from CTD bottles (0 to 300 m) and from the surface seawater intake as described above, spiked with a <sup>230</sup>Th yield monitor, precipitated in MnO<sub>2</sub>, filtered onto quartz microfiber filters, and mounted for beta counting as described by Pike et al. [2005]. Samples were returned to shore

**Table 1.** Summary of Sampling Transects

| Transect ID | Date and Time (GMT) | Mixed-Layer Mean, Range (m) <sup>a</sup> | PPZ Depth Mean, Range (m) <sup>a</sup> | Mixed-Layer NCP Mean, SD (mmol C m <sup>-2</sup> d <sup>-1</sup> ) <sup>a,b</sup> | Mixed-Layer EP Mean, SD (mmol C m <sup>-2</sup> d <sup>-1</sup> ) <sup>a,b</sup> | Production Zone EP Mean, SD (mmol C m <sup>-2</sup> d <sup>-1</sup> ) <sup>a,b</sup> | Mixed-Layer EP:NCP R Value <sup>c</sup> | Mixed-Layer EP:NCP p Value <sup>c</sup> |
|-------------|---------------------|--|--|---|--|--|---|---|
| 2011 #1     | 9/30/11 18:06       | 35.5 (21)                                | 132.5 (89)                             | NA  | 3.6 (2.1)  | 6.1 (0.5)  | NA                                      | NA                                      |
| 2011 #2     | 10/4/11 0:19        | 37 (6)                                   | 130 (6)                                | 1.1 (0.6)   | 0.7 (0.9)  | 1.3 (0.7)  | -0.40                                   | 0.16                                    |
| 2011 #3     | 10/5/11 21:30       | 42.5 (27)                                | 178.5 (13)                             | 1.9 (0.2)   | 0.7 (1.4)  | 1 (0.9)  | 0.25                                    | 0.41                                    |
| 2011 #4     | 10/9/11 23:45       | 46 (6)                                   | 197.5 (11)                             | NA  | 1.0 (1.5)  | 0.7 (0.9)  | NA                                      | NA                                      |
| 2011 #5     | 10/11/11 0:22       | 45 (10)                                  | 187 (16)                               | 2.2 (0.4)   | 1.0 (1.4)  | -0.6 (2.3)   | <b>0.57</b>                             | <b>0.04</b>                             |
| 2011 #6     | 10/11/11 21:46      | 47 (4)                                   | 214 (26)                               | 1.5 (0.4)   | 1.3 (1.2)  | 1.5 (0.4)  | -0.58                                   | 0.03                                    |
| 2012 #1     | 9/27/12 22:09       | 42.5 (5)                                 | 153 (60)                               | 3.4 (0.5)   | 2.3 (0.9)  | 3 (0)  | -0.12                                   | 0.61                                    |
| 2012 #2     | 9/28/12 23:44       | 44.5 (5)                                 | 146.5 (19)                             | 2.2 (0.4)   | 2.3 (1.3)  | 3.4 (0.1)  | -0.09                                   | 0.71                                    |
| 2012 #3     | 9/30/12 7:20        | 40 (8)                                   | 150 (6)                                | 2.5 (0.2)   | 2 (0.8)  | 2.8 (0.5)  | 0.38                                    | 0.11                                    |
| 2012 #4     | 10/2/12 18:26       | 30.5 (13)                                | 171.5 (33)                             | 1.6 (0.6)   | 1.6 (1.1)  | 1.6 (0.1)  | -0.14                                   | 0.57                                    |

<sup>a</sup>Standard deviations are computed across all surface samples, while ranges are between the two endpoint CTDs.

<sup>b</sup>EP at the base of the mixed layer is estimated from single-surface bottles, while EP at the production zone depth is integrated over a CTD cast. C:<sup>234</sup>Th ratios were estimated at the integration depth (mixed layer or PPZ) from the Owens et al. [2015] data set.

<sup>c</sup>Correlation coefficients and p values are computed across each transect using mixed-layer NCP measurements subsampled to locations of EP measurements. Instance of significant (95% confidence), positive correlation between NCP and EP is shown in boldface.

for initial beta counting within 15 days of collection, then recounted to determine background beta decay rates after passage of at least six <sup>234</sup>Th half-lives ( $\tau_{1/2} = 23.1$  days). Precipitates were finally digested, spiked with <sup>229</sup>Th, and the ratio of <sup>230</sup>Th/<sup>229</sup>Th in the filtered digest determined via inductively coupled plasma-mass spectrometry [Pike et al., 2005; Owens et al., 2015]. The processing recovery by this method averaged 83% for the 2011 samples and 92% in 2012.

The <sup>234</sup>Th deficit was computed relative to the salinity-derived, parent <sup>238</sup>U activity [Owens et al., 2011]. Propagated counting errors, uncertainties in the <sup>230</sup>Th/<sup>229</sup>Th ratio, and uncertainty in the salinity:<sup>238</sup>U relationship are combined in the <sup>234</sup>Th deficit uncertainties reported below. <sup>234</sup>Th deficit profiles were integrated in three ways: (1) from CTD profiles, from surface to the PPZ depth, (2) from the top few CTD bottles, from surface to the base of the mixed layer, and (3) from single-surface CTD bottles and surface underway samples, integrated to the base of the mixed layer. The latter two integration methods allowed comparison to surface underway measurements of mixed-layer O<sub>2</sub>/Ar (described below).

Export production was computed by assuming a steady state decay model and negligible advection and diffusion of <sup>234</sup>Th [Coale and Bruland, 1987]. To calculate EP in carbon units, the <sup>234</sup>Th flux is multiplied by the particulate C:<sup>234</sup>Th ratio typically collected via size-fractionated particles filtered with in situ pumps or particles collected in sediment traps [Buesseler et al., 2006]. However, we were not able to directly measure the C:<sup>234</sup>Th ratio due to time constraints. Instead, we used a comprehensive data set of depth-resolved, large-particle C:<sup>234</sup>Th from the subtropical North and South Atlantic to estimate the C:<sup>234</sup>Th ratios of sinking particles [Owens et al., 2015] at our mixed-layer and PPZ depths. Carbon export fluxes compared below to NCP include all propagated uncertainty sources, including the predicted C:<sup>234</sup>Th ratio, which was often the largest source of uncertainty. Uncertainty due to the assumption of a steady state model is further discussed below in section 4.4.

### 2.5. O<sub>2</sub>/Ar Ratio and NCP

The O<sub>2</sub>/Ar ratio was measured continuously from surface seawater using an equilibrator inlet mass spectrometer (EIMS) [Cassar et al., 2009], while calibration O<sub>2</sub>/Ar bottle samples were collected from the surface seawater supply and from CTD

bottles. Those discrete samples were analyzed at Woods Hole Oceanographic Institution on a 253 MAT isotope ratio mass spectrometer, following the method of Barkan and Luz [2003]. The EIMS seawater intake was plumbed into the ship's underway seawater sampling line. A detailed description of the EIMS system and its calibration against bottle samples can be found in *Stanley et al.* [2010]. O<sub>2</sub>/Ar samples taken from the underway seawater sampling line at same time as CTD samples were collected confirmed that there was no significant biological respiration within the ship's underway line. NCP data were not available from 2 of the 10 transects (2011 #1 and #4 in Table 1) due to bubble entrainment into the seawater line during rough conditions.

Biological oxygen saturation was computed as the ratio of O<sub>2</sub> saturation relative to that of Ar. NCP was then calculated as the product of the biological oxygen saturation, gas-transfer velocity, and oxygen concentration by assuming steady state and minimal effect of advection and diffusion. The NCP computation is described in detail in *Stanley et al.* [2010]. Wind fields (6 hourly) from the NCAR/NCEP reanalysis model for the previous 30 days [*Kalnay et al.*, 1996] were used to estimate weighted average gas-transfer velocities [*Reuer et al.*, 2007]. A gas exchange parameterization that had been derived from data from the Sargasso Sea was used [*Stanley et al.*, 2009]. Results were similar if other gas exchange parameterizations were used instead [*Ho et al.*, 2006; *Nightingale et al.*, 2000; *Wanninkhof*, 1992]. Uncertainty in parameterization of the gas-transfer coefficient is estimated to lead to a  $\pm 15\%$  uncertainty in computed NCP [*Stanley et al.*, 2009]. We used a photosynthetic quotient of 1.4 [*Laws*, 1991] to convert NCP from oxygen to carbon units. Since sampling was conducted in autumn, NCP estimates were also corrected for entrainment of deeper waters into the mixed layer prior to sampling. Argo float-observed mixed-layer depths were interpolated from the Japan Agency for Marine-Earth Science and Technology Mixed Layer data set of Argo, Grid Point Value data set [*Hosoda et al.*, 2010] to locations and times 10 days prior to sampling. Changes in mixed-layer depths and submixed-layer O<sub>2</sub> concentrations from CTD casts were used to compute corrections to NCP estimates. Entrainment corrections were less than  $\pm 6\%$  of the uncorrected NCP value in all transects except 2011 #3, where it was 23% of the uncorrected NCP.

## 2.6. Particulate Biogeochemical Properties

Seawater samples for analysis of phytoplankton pigments by HPLC were collected from the surface seawater line at a subset of surface sampling locations and from a subset of CTD bottles. Samples were filtered onto precombusted GF/F filters and then frozen at  $-80^{\circ}\text{C}$  until analysis by HPLC [*Hooker et al.*, 2005] (NASA Goddard Space Flight Center (GSFC) Ocean Ecology Laboratory; <http://oceancolor.gsfc.nasa.gov/HPLC/>).

Two-liter POC/PON samples were collected from the surface seawater line and from CTD bottles and filtered onto precombusted Whatman GF/F filters (450°C for 4 h) and stored frozen ( $-20^{\circ}\text{C}$ ) in combusted glass vials until analysis. For analysis, filters were dried overnight at  $60^{\circ}\text{C}$ , acidified overnight to remove carbonate salts, and redried at  $60^{\circ}\text{C}$  before packing in combusted nickel sleeves. Samples were analyzed on a Control Equipment 440-XA elemental analyzer [*Lomas et al.*, 2013].

Samples for picoplankton enumeration were collected from the underway system and analyzed via flow cytometry as in *Lomas et al.* [2010]. Briefly, cryo vials were rinsed with sample before samples were fixed with paraformaldehyde (0.5% final concentration), stored at  $-4^{\circ}\text{C}$  for 1–2 h, before long-term storage in liquid nitrogen. Samples were analyzed on a Becton Dickinson (formerly Cytopeia Inc.) Influx cytometer using a 488 nm blue excitation laser, appropriate Chl-*a* ( $692 \pm 20$  nm), and phycoerythrin ( $580 \pm 15$  nm) band-pass filters was calibrated daily with  $0.53 \mu\text{m}$  and  $2.88 \mu\text{m}$  fluorescent microbeads (Spherotech Inc. Libertyville, Illinois, USA). Each sample was run for 4–6 min ( $\sim 0.2$ – $0.3$  mL total volume analyzed), with log-amplified Chl-*a* and phycoerythrin fluorescence, and forward and right-angle scatter signals were recorded. Data files were analyzed from two-dimensional scatterplots based on red or orange fluorescence and characteristic light-scattering properties [e.g., *DuRand and Olson*, 1996] using FCS Express 3.0 (DeNovo Software Inc. Los Angeles, California, USA). Picoautotrophs were identified as either *Synechococcus* or *Prochlorococcus* based upon cell size and the presence or absence of phycoerythrin, respectively. Based upon these gating criteria, the number of cells in each identified population was enumerated and converted to cell abundances by the volume-analyzed method [*Sieracki et al.*, 1993]. Precision of triplicate samples was generally  $<5\%$  for cell concentrations  $>200$  cells  $\text{mL}^{-1}$ .

Samples were collected from the surface seawater line for size-fractionated chlorophyll analysis. Four-liter volumes were filtered through  $5.0 \mu\text{m}$  polycarbonate membrane filters (Nuclepore), and in 2011, 1 L samples

were divided and filtered in parallel through GF/F and 0.2  $\mu\text{m}$  polycarbonate membrane filters (Nuclepore). During the 2012 cruise, 1 L samples were instead filtered sequentially through GF/F and 0.2  $\mu\text{m}$  filters. All filters were frozen at  $-80^\circ\text{C}$ , extracted in acetone at  $-20^\circ\text{C}$ , and chlorophyll fluorescence determined on a Turner TD-700 fluorometer before and after acidification with 10% HCl [Strickland and Parsons, 1972]. In both sampling years, concentrations of chlorophyll on 0.2  $\mu\text{m}$  filters were not detectably different than on GF/F filters, suggesting either negligible chlorophyll between 0.2  $\mu\text{m}$  and the nominal GF/F cutoff of 0.7  $\mu\text{m}$  or (more likely) clogging of the GF/F filter so that the true cutoff was closer to 0.2  $\mu\text{m}$ . Below, we therefore discuss only the GF/F – 5.0  $\mu\text{m}$  (“small-sized”) and  $>5.0 \mu\text{m}$  (“large-sized”) chlorophyll size classes.

Acidification of the first batch of filters analyzed in 2011 was apparently incomplete, as evidenced by low unacidified-to-acidified fluorescence ratios ( $F_o/F_a$ ). This could have been due to high chlorophyll-b concentrations [Welschmeyer, 1994], but HPLC results showed negligible concentrations of this pigment. However, HPLC phaeopigment concentrations in surface samples were also negligible, and HPLC chlorophyll-a was well correlated to unacidified, GF/F chlorophyll fluorescence. Thus, for 2011 samples, fluorometric chlorophyll concentrations were calculated from unacidified readings and then calibrated against HPLC chlorophyll-a concentrations.

Seawater samples for TEP analysis, ranging from 0.2 to 0.3 L, were filtered at low pressure in triplicate onto 0.4  $\mu\text{m}$  polycarbonate membrane filters (Sterlitech), rinsed with Milli-Q water, stained with 0.02% Alcian Blue, rinsed again, and frozen at  $-20^\circ\text{C}$ . On shore, filters and stained particulates were digested in 80%  $\text{H}_2\text{SO}_4$  and the stain concentrations were determined spectrophotometrically as described by Engel [2009]. The stain was calibrated against standard suspensions of Xanthan gum within 6 weeks of use and stored at  $4^\circ\text{C}$ . The detection limit was 10  $\mu\text{g}$  Xanthan equivalent  $\text{L}^{-1}$  ( $\text{Xeq L}^{-1}$ ). Reported TEP concentrations are the mean of three replicates.

### 3. Results

The targeted transects tended to have strong surface horizontal temperature and salinity gradients and vertical density displacements between the two endpoint CTDs (Table 1; Figures 3–5 show detailed data plots for transects 2011 #5–6 and 2012 #2; all other transects are shown in the supporting information Figures S2–S8). The single exception to this was transect 2011 #4 (supporting information Figure S5). In general, the magnitudes of biogeochemical parameters, NCP, and export were consistent with low-surface productivity conditions characteristic of the stratified, oligotrophic ocean in early autumn (Table 1 and Figures 3–5). In spite of these conditions, biogeochemical parameters exhibited substantial variability at the surface at 2 km spatial resolution, the smallest observable scale for discrete samples. Only in transect 2011 #1, near the Gulf Stream wall, did surface chlorophyll concentrations consistently exceed  $\sim 0.1 \text{ mg m}^{-3}$  (supporting information Figure S2). Surface sample cell counts for *Synechococcus*, picoeukaryotes, and nanoeukaryotes were low and in many cases exhibited high variability between replicates, while counts for *Prochlorococcus*, as expected, were significantly higher. Surface organic particulate C:N ratios ranged from less than 6 to greater than 10. TEP concentrations ranged from below detectability up to 200  $\mu\text{g}$  Xanthan equivalent  $\text{L}^{-1}$ . Transect-averaged, mixed-layer export ranged from 0.7 to 3.6  $\text{mmol C m}^{-2} \text{ d}^{-1}$  and NCP from 1.1 to 3.4  $\text{mmol C m}^{-2} \text{ d}^{-1}$  (Table 1). Averaged across the individual transects, export was approximately equal to or less than NCP, while within-transect variability was higher for EP than NCP (Table 1 and Figure 6).

Along-transect spatial coherence among physical and various biogeochemical parameters at scales  $\leq 10 \text{ km}$  was common, but rarely did the same parameters covary for different transects, and in no case did all parameters covary within a single feature. In transect 2011 #5, salinity, chlorophyll in both size classes, TEP, and export were all locally depressed over a midtransect, 2–4 km range (Figure 3). In transect 2011 #6, TEP, export, and the particulate C:N ratio were depressed over a 1–2 km range centered at about 20 km along transect, while NCP and both chlorophyll size classes were higher over a broader  $\sim 10 \text{ km}$  spatial range centered at about 10 km along transect (Figure 4). In transect 2012 #2, colocated minima and maxima were observed in *Prochlorococcus* counts and small-sized chlorophyll (Figure 5). Other features show similar patterns of transient coherence among biogeochemical parameters at sub 10 km spatial scales (see supporting information).

In several cases, patterns of variability at submesoscales (here  $\leq 10 \text{ km}$ ) were superimposed over larger-scale spatial gradients such as those encountered crossing in and out of mesoscale eddies or for other large-scale circulatory features (i.e., the Gulf Stream). In transects 2012 #2 (Figure 5) and 2012 #1 and #3 (supporting information

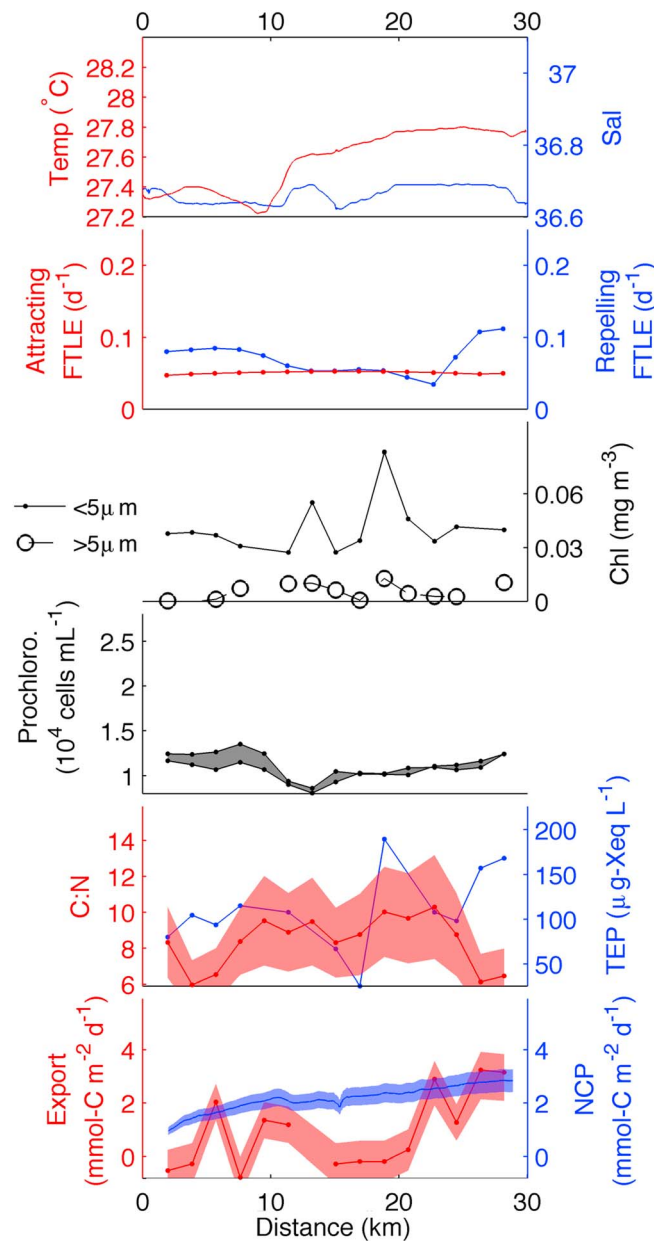


**Figure 3.** Surface transect 2011 #5. (first panel) Temperature (red, left) and salinity (blue, right). (second panel) Modeled FTLE surfaces, both attracting (red, left) and repelling (blue, right). Along-transect locations of FTLE values should be interpreted with caution (see text). (third panel) Fluorometric chlorophyll-a in  $<5\ \mu\text{m}$  (points/solid line) and  $>5\ \mu\text{m}$  (open circles/dashed line) size classes. (fourth panel) *Prochlorococcus* cell counts in two replicate samples (upper and lower bounds of gray fill). (fifth panel) C:N ratio of particulate material and propagated analytical uncertainty (red line/fill, left) as well as TEP concentration (blue, right). (sixth panel) Export derived from surface  $^{234}\text{Th}$  deficit (red, left) and NCP derived from surface  $\text{O}_2\text{:Ar}$  ratios (blue, right). Red fill shows effect of varying predicted C: $^{234}\text{Th}$  ratio through 95% confidence range, while blue fill shows  $\pm 15\%$  uncertainty in gas-transfer velocity. Note sharp, collocated minima ( $\sim 18\ \text{km}$ ) in salinity, both chlorophyll size fractions, TEP concentration, export, and generally good correspondence of TEP and large chlorophyll.

Figures S5 and S7), the locations of predicted, repelling FTLE ridges encircled a cyclonic eddy (Figure 7 and supporting information Figure S1). Spatial banding in small-sized chlorophyll occurred at similar scales to banding in FTLE surfaces (Figure 7). In transect 2012 #2 (Figure 5), likely mesoscale eddy-associated gradients in temperature, salinity, *Prochlorococcus*, TEP, and NCP were visible over scales of 10 km, with superimposed fluctuations at  $<10\ \text{km}$  scales. In transect 2011 #1 (supporting information Figure S2), very steep mid-transect gradients in temperature, salinity, *Prochlorococcus*, and small-sized chlorophyll were associated with the Gulf Stream wall, as well as variations in TEP, export, and large-sized chlorophyll.

To quantify surface variability along transects crossing LCS features, we computed the coefficient of variability (CV) for biogeochemical and flux parameters (defined as the standard deviation-to-mean ratio of along-transect surface observations). CV values for large-sized chlorophyll concentrations and EP are of order 1 and often larger demonstrating a large degree of submesoscale variability for those quantities (Figure 8). Small-sized chlorophyll and NCP consistently had smaller CVs than did large-sized chlorophyll and export. Coefficients of variation for *Prochlorococcus* cell counts, POC, and TEP are not shown in Figure 8 for clarity. However, values of the first two parameters were similar to NCP and small-sized chlorophyll, while values for TEP were larger, similar to large-sized chlorophyll and export. The expected CV magnitude due solely to analytical variability was also computed for each parameter and transect using a Monte Carlo procedure in which each parameter's measurement uncertainty was used to generate normally distributed "noise" around each set of transect samples. The variability in the CVs computed for each of many such trials was usually much smaller than the across-transect CV (Figure 8). The CV for export was larger than that for NCP in all transects.

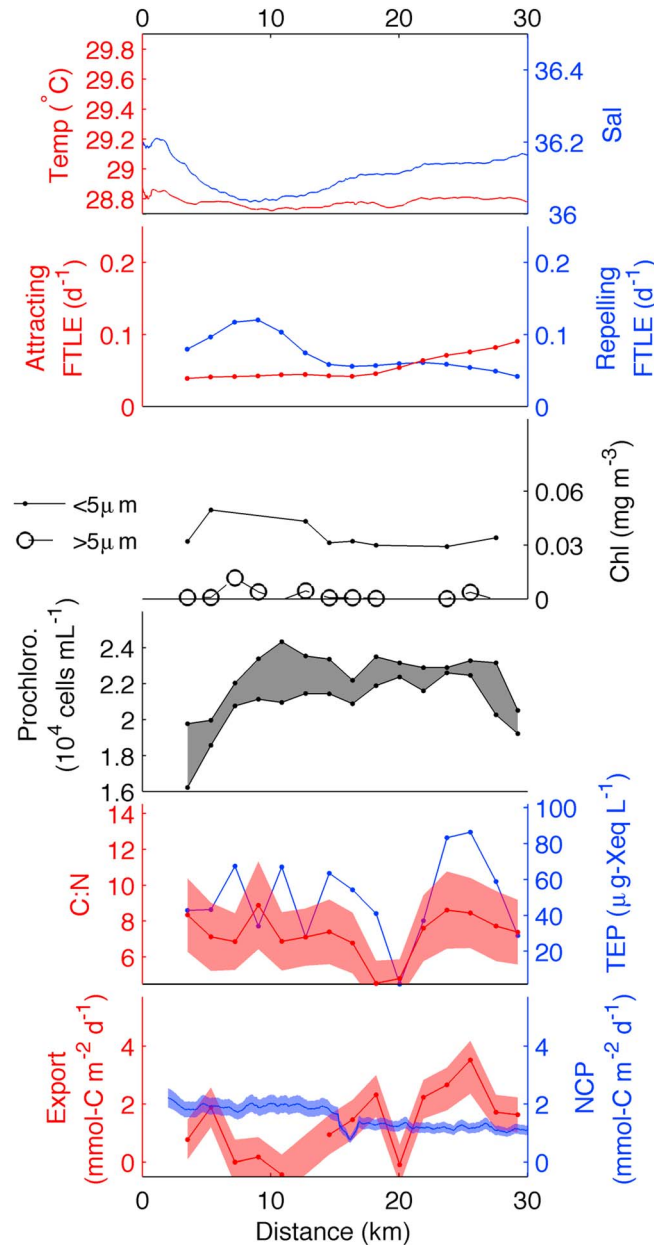


**Figure 4.** Surface transect 2011 #6. Panel layouts are the same as Figure 3. Note collocation of salinity minimum, FTLE “repeller” maximum, maxima in both chlorophyll fractions, and higher NCP in first half of transect. Also note covariance of TEP, C:N ratio, and export in second half of transect.

across large spatiotemporal scales is apparent only after averaging over each high-resolution transect, and the transect variability in EP exceeds that in NCP. Both findings suggest the decoupling of processes controlling EP and NCP. Net community production nonetheless appears to place an upper limit on EP over large scales, with some production presumably going into the DOC pool. While we did not observe ubiquitous controls on export, such as TEP aggregation, our results do suggest that the observed, strong variability in carbon fluxes on submesoscales is likely common in the ocean.

#### 4.1. Sampling Upper Ocean Carbon Fluxes at Submesoscale Features

Near-real-time remote sensing observations and calculations of FTLEs allowed targeting of SMS features for field sampling. Qualitative assessment of surface variability in temperature and salinity (Figures 3–5 and

Export values derived from single-bottle surface  $^{234}\text{Th}$  deficits were well correlated to export measured at the PPZ depth ( $R^2 = 0.72$ ,  $n = 20$ ), similar to observations at the West Antarctic Peninsula by Owens [2012] (Table 1 and Figure 9). The regression line between C export at the base of the mixed layer and at the base of the PPZ had a negative intercept (Figure 9). Measured at 2 km resolution across single transects, mixed-layer NCP and export were nearly all poorly correlated at the 95% confidence level (Table 1). Only in one case (2011 #5) were paired, 2 km observations of NCP and export significantly correlated within a single transect, although the critical values of  $R$ , for  $N = 15$  and 20, are respectively 0.43 and 0.37 at the 95% confidence level, so our observations do not test for weak correlations. However, export and NCP were well correlated when averaged values are compared over all transects ( $R = 0.72$ ,  $p = 0.04$ ; Figure 10).

#### 4. Discussion

Several major conclusions arise from our observations as we discuss below. First, we were able to locate submesoscale (SMS) physical features from near-real-time satellite imagery and satellite altimetry-based FTLE observations. The high variability in measured, biogeochemical parameters and carbon fluxes, and the lack of ubiquitous relationships among those parameters and fluxes, suggests a diversity of controls on upper ocean carbon cycling. We show below that the depth of integration must be considered when comparing carbon fluxes measured by different methods. The strong correlation of EP and NCP

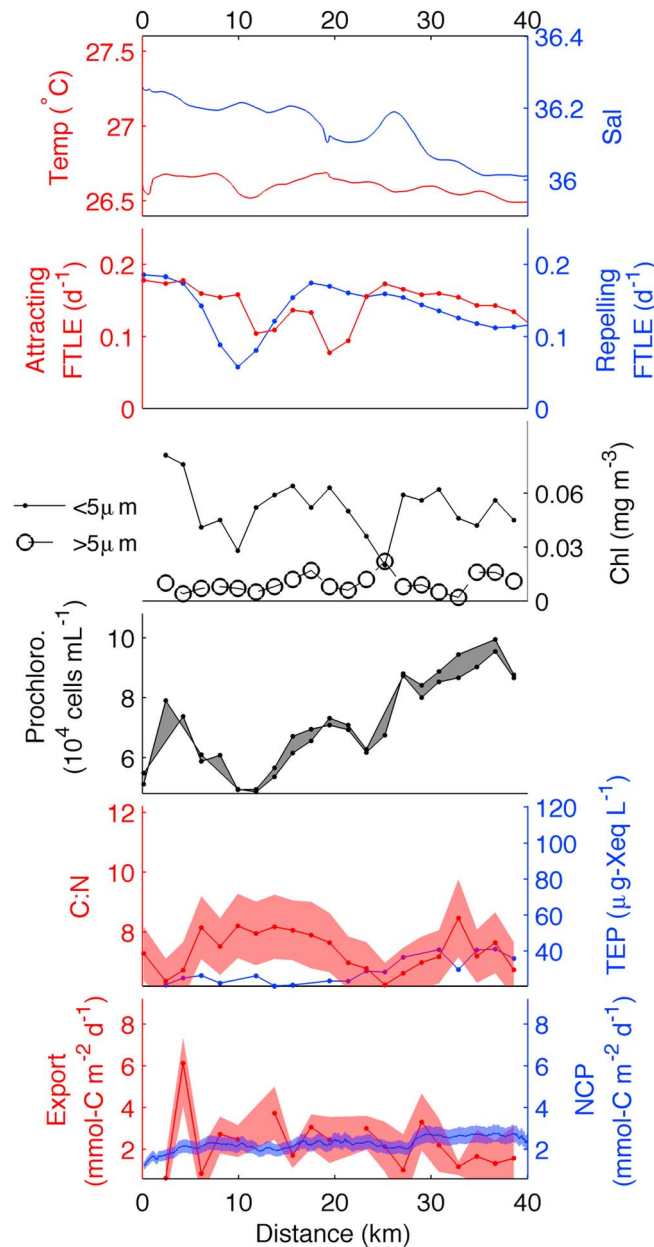


**Figure 5.** Surface transect 2012 #2. Panel layouts are the same as Figures 3 and 4. Note large magnitude of oscillations in T, S, both chlorophyll size fractions, *Prochlorococcus*, NCP, and export.

the surface over short (<10 km) spatial scales without covarying with one another. In other cases, most notably feature 2011 #5 (Figure 3), coincident local maxima in chlorophyll, NCP, and diverging FTLE fields suggested connections among submesoscale physics, primary production, and carbon cycling response. To the extent that such decoupling is ubiquitous within the ocean, full characterization of the state of the biological pump for a given region and time will require a four-dimensional sampling plan that samples the time-evolution of these SMS features and their biogeochemical impacts.

**4.2. Depth Dependence of Ocean Carbon Fluxes**

We found a strong relationship between export at the surface and export integrated through the euphotic zone (Figure 9). However, the fraction of total export contributed by the mixed layer varied strongly, even

supporting information) shows that we encountered the expected sharp physical gradients in 9 out of 10 target features (the lone exception was 2011 #4). The present approach nearly always found strong physical gradients with associated strong variations in biogeochemical properties, but we also observed biogeochemical variability in the absence of SMS activity (2011 #4, supporting information Figure S5), suggesting many different reasons for variability of biogeochemical processes in the ocean.

The available data are not useful for testing the hypothesis that biogeochemical hot spots are always associated with regional submesoscale activity, as the transects were located to maximize SMS variability. Detailed, long-transect observations encompassing areas of strong and weak SMS variabilities and testing biogeochemical activity over a range of spatial scales are required. The observations were also not useful for exploring biogeochemical variability at scales smaller than 2 km.

The present observational data set sampled each frontal transect at a given instant in time. Numerical model results suggest that individual SMS features evolve on time scales of days to weeks [Lévy *et al.*, 2012]. Hence, the biogeochemical processes are not likely at steady state during any one of our frontal transect snapshots (Figure 1). As has been noted above, we did not find spatial patterns in the measured biogeochemical and carbon flux parameters sampled that permitted a simple diagnosis of relevant processes. In some cases, such as feature 2012 #2 (Figure 5), most parameters showed strong variability at

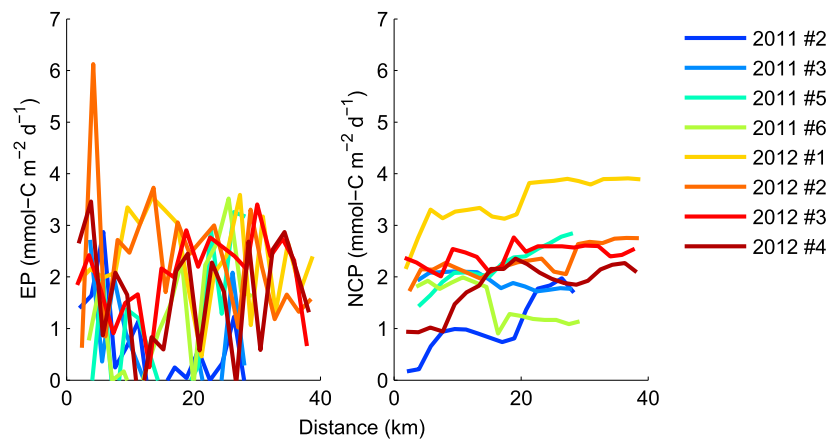


**Figure 6.** Summary of all mixed-layer (left) export and (right) NCP transects from bottom panels of Figures 3–5 and supporting information Figures S2–S8. Colors serve only to distinguish transects from one another. Variability in EP over short distances is clearly higher than in NCP.

between endpoint CTD casts of the same transect. This is consistent with the observed, strong variability in export and with the changing controls on new production during the early fall in the Sargasso Sea. For instance, *Fawcett et al.* [2014] found eukaryotic  $\delta^{15}\text{N}$  values indicating periodic instances of enhanced new production below the mixed layer during measurements made from July through December. In contrast, *Luz and Barkan* [2009] used oxygen isotopic compositions and  $\text{O}_2/\text{Ar}$  saturation to show that the mixed-layer accounts for a larger fraction of integrated gross oxygen production at BATS during September and October than it does during early or late summer (51% versus 25%). While we do not have submixed-layer NCP measurements here, the depth dependence of net primary production (NPP) is likely to be similar to NCP if heterotrophic respiration is at least proportional to NPP if not constant with depth. We used early-autumn  $^{14}\text{C}$  net primary production data from the BATS archive (1988–2010; batsftp.bios.edu) to compare the mixed-

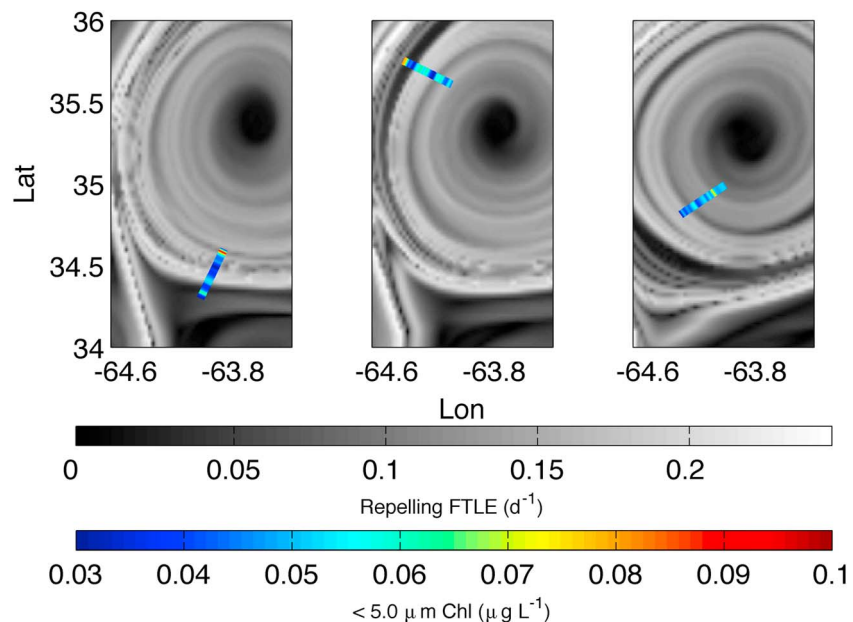


**Figure 7.** Chlorophyll-a ( $<5 \mu\text{m}$ , colors) overlaid on modeled repelling FTLE surfaces (gray scale) for 2012 transects (left) #1, (middle) #2, and (right) #3. Because modeled FTLE determinations are based upon mapped satellite sea level fields, the correspondence with field sample locations is approximate at best. However, exact alignment between chlorophyll and FTLE bands is unimportant; rather, the maps illustrate similar scales of surface variability between the submesoscale physical forcing and the biological response.

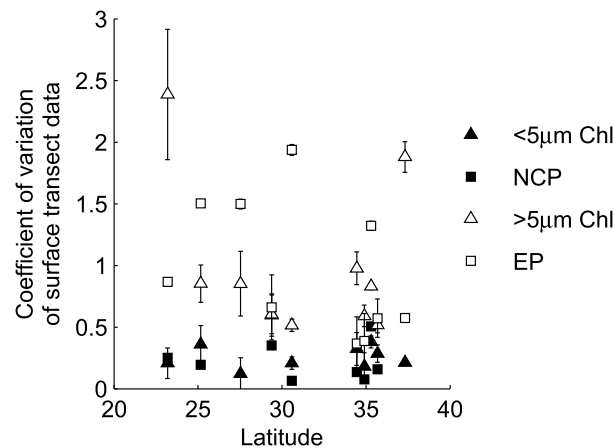


**Figure 8.** Coefficients of variation (CV) of size-fractionated chlorophyll, NCP, and export across 30 and 40 km surface transects, arranged by center latitude. Chlorophyll at small sizes and NCP (black symbols) show less spatial variability than do large-sized chlorophyll and export (white symbols). Vertical error bars show variability in CV introduced via addition of normally distributed “analytical noise” (see text).

Net community production and export should, by definition, be equal to one another when integrated over large spatiotemporal scales. Our measurements should not reflect vertical decoupling of NCP and export because we estimated both fluxes at the base of the mixed layer. The lack of observable correlation of NCP to export within single transects (Table 1, Figure 6) or across the ensemble of paired observations (Figure 10a) suggests that different ecosystem processes and trophic levels must control net production and export, leading to spatial decoupling on horizontal scales of a few kilometers. There is no sense of progression of ecosystem processes in these fluxes along our sampling transects as we are randomly sampling them across the targeted fronts.

We do find significant and positive correlations between NCP and EP when individual estimates are averaged over 30 or 40 km sampling transects (Table 1 and Figure 10b). The correlation between the transect-averaged, mixed-layer fluxes is highly significant ( $R=0.72$ ;  $p=0.04$ ). We evaluated whether this correlation is simply happenstance by resorting the individual, paired observations (supporting information Table S1) randomly into eight transects and calculated regression statistics over 5000 trials. We found that for 9.3% of the trials, the significance levels for the regression between the resorted EP and NCP transect averages were better than the sampled transect averages. Hence, the strong and significant correlations between the sampled transect averages of EP and NCP are not likely to be the result of simple chance.

The slope of regression between the transect-averaged EP and NCP also holds important information. We find that the slope of the Type-II regression of particulate export against NCP is 0.93, slightly less than the theoretical value of one but not significantly different (standard deviation = 0.32,  $t$  test, symmetrical 95% confidence limits). This is consistent with the idea that net production places an upper limit on export from the production zone. As we discuss below, however, the physical and biological mechanisms leading to export are likely decoupled from those that control net community production.

#### 4.4. Scales of Spatial and Temporal Variability

A number of researchers have used techniques such as spectral analysis, autocorrelation, and semivariograms to describe the spatial variability in various modeled and observed parameters as a function of length scale [Denman and Platt, 1976; Abraham, 1998; Martin, 2003]. They have found generally that physical parameters have the “steepest” power spectra—i.e., containing larger amounts of variability at larger spatial scales. On the other hand, biological parameters (e.g., chlorophyll concentration or zooplankton abundance) have flatter spectra, with more variability at shorter spatial scales. Because nonlinearities arise during ecosystem interactions, higher trophic levels are thought to have increasingly more small-scale variability [Mackas and Boyd, 1979; Garçon et al., 2001; Levy and Martin, 2013]. While our discretely sampled, surface transects were too short to allow extraction of spatial information by spectral methods, across-transect coefficients of variation (CVs)

layer and euphotic zone NPP during the late September to early October period of the year (Figure 9). Similar to export, there is a variable contribution of the mixed layer to integrated NPP. Finally, we found that transect-averaged, mixed-layer NCP and export integrated to the PPZ depth (the former from underway measurements, the latter from CTD casts) were not significantly correlated across all transects (Table 1;  $R=0.47$ ,  $p=0.24$ ). These results reinforce the importance of measuring NCP and export at the same depth and integrating both fluxes to the same depth, if they are to be compared.

#### 4.3. Relationship Between Upper Ocean Net Community and Export Production

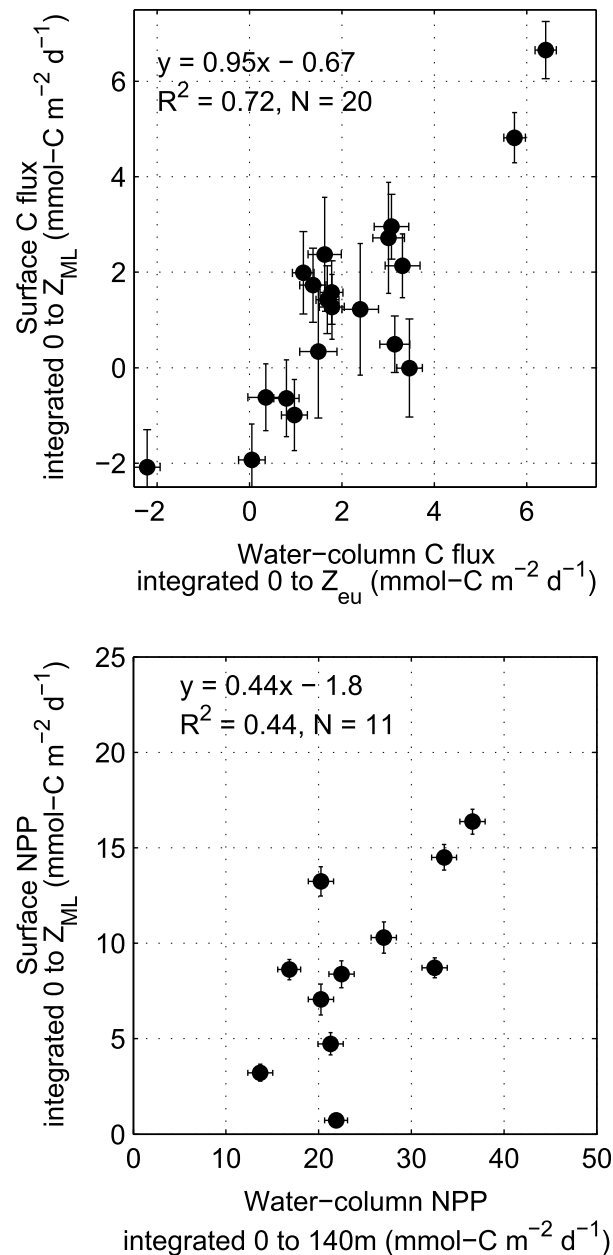


**Figure 9.** (left) Comparison of  $^{234}\text{Th}$ -derived C export fluxes integrated down to the base of the particle production layer versus to the base of the mixed layer. Uncertainties are propagated from counting error. (right) Comparison of all BATS time series NPP measurements between 27 September and 11 October, integrated to 140 m versus to the base of the mixed layer. Uncertainties are propagated from the time series mean standard deviation among replicates. Both C export and NPP have negative y intercepts, suggesting smaller contributions of the mixed layer to the integrated flux when total flux is low.

response time at steady state. Our measured  $^{234}\text{Th}$  deficits likely reflect temporal (i.e., nonsteady state) as well as spatial changes in the ecosystem. However, two lines of evidence suggest that spatial gradients influenced the observed export variability more than temporal changes that occurred prior to sampling. First, the observed CV values for the large-sized chlorophyll fraction approached and sometimes exceeded those for export (Figure 8). Cellular chlorophyll concentrations equilibrate quickly with environmental conditions [e.g., Geider, 1987], so the CV for large-sized chlorophyll probably reflects mostly spatial variability. Second, *Resplandy et al.*

provide a simple measure of relative variability at the 30–40 km length scale (Figure 8). Consistent with the idea of nonlinear ecosystem processes introducing variability at smaller and smaller scales as trophic level increases, we also saw CVs increase for the large-sized chlorophyll fraction, for TEP, and for carbon export, perhaps due to a greater influence of higher trophic level interactions governing variability in these parameters. A surprising finding was that spatial variability in export appears to be larger than that of NCP at the 30–40 km length scale (Figure 8). This provides support for the present conceptual model (Figure 1) that NCP and export are spatially and perhaps temporally decoupled, possibly due to their control by different trophic levels with different scales of spatiotemporal variability [Mackas and Boyd, 1979; Garçon et al., 2001; Lévy and Martin, 2013]. Our observations leave open the possibility that such decoupling is not only to be expected in the vicinity of strong, submesoscale physical gradients, which present barriers to horizontal mixing, but might be characteristic in general.

The mean lifetime of a particle-reactive, radioactive element is governed both by the rate of scavenging and export on particles and the rate of radioactive decay. For  $^{234}\text{Th}$ , the steady state response time in a given parcel is shorter than its mean life with respect to decay because of scavenging on sinking particles [Turnewitsch et al., 2008]. Our intentional sampling of strong physical gradients, which are predicted to have elevated submesoscale energy and thereby rapidly evolving biogeochemical responses [e.g., Lévy et al., 2012], makes it possible that the scavenging rate for  $^{234}\text{Th}$  on sinking particles was faster than the  $^{234}\text{Th}$  decay rate. Therefore, the actual response time for  $^{234}\text{Th}$  would be shorter than its 35 day

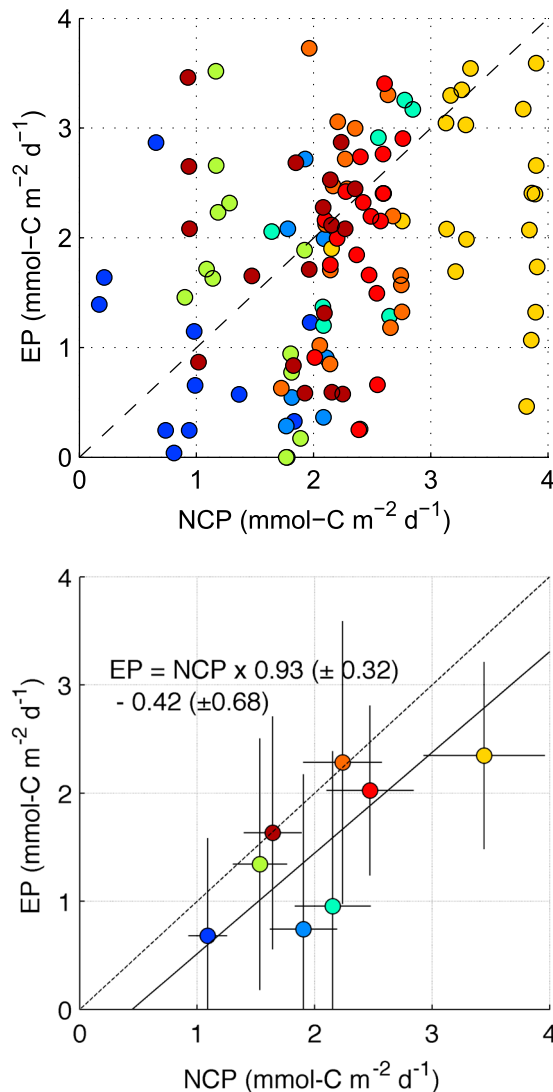


**Figure 10.** (top) Mixed-layer export versus entrainment-corrected NCP individual measurements across transects are shown without averaging. Colors differentiate transects from one another and correspond to the legend in Figure 6. Dashed line shows 1:1 relationship. (bottom) As in Figure 10 (top) but NCP and EP are averaged across surface transects. Each dot shows one transect. Error bars show  $\pm 1$  standard deviation measured across each transect. The 1:1 line (dashed) is also shown for reference. Type-II linear fit (solid line) between EP and entrainment-corrected NCP is:  $EP = NCP \times 0.93 - 0.42$  ( $\text{mmol}^{-1} \text{C m}^{-2} \text{d}^{-1}$ ),  $R = 0.72$ ,  $\rho = 0.04$ ,  $n = 8$ .

#### 4.6. Carbon Budget Uncertainties

There are a few possible sources of uncertainty and bias in the EP:NCP relationship, which bear discussion. The first is the uncertainty stemming from our estimated  $\text{C}^{234}\text{Th}$  ratios, which were extrapolated from a depth-resolved, basin-wide data set collected primarily in the late autumn [Owens *et al.*, 2015]. However, both the source  $\text{C}^{234}\text{Th}$  data set and our transects were collected in the same season in the oligotrophic Atlantic, away from coasts and productive, high-latitude settings, and are thus expected to have similar depth and particle size dependences [Buesseler *et al.*, 2006]. The source  $\text{C}^{234}\text{Th}$  data set's spatial breadth increases the probability of it representing the various conditions encountered during transects sampled here. A second source of uncertainty is temporal decoupling of NCP and export in the vicinity of strong

[2012] used a submesoscale-resolving, dynamical-biogeochemical model of  $^{234}\text{Th}$  activity to address precisely this question, and they found that small-scale spatial gradients in  $^{234}\text{Th}$  activity tended to persist within filamentous, submesoscale features through the lifetime of the tracer, rather than being mixed and homogenized.

#### 4.5. Role of TEP in Aggregation and Export

Previous researchers have separately found TEP concentrations to correlate well with chlorophyll concentrations [Passow, 2001], to form specific chemical associations with  $^{234}\text{Th}$  [Quigley *et al.*, 2002; Passow *et al.*, 2006], and to play a role in formation of sinking aggregates, thus possibly contributing to carbon export [Passow, 2001; Martin *et al.*, 2011]. We observed all of these relationships at subtransect scales (Figures 3 and 4) but not consistently (Figure S5, supporting information) This suggests that the role of TEP in aggregation and export may evolve over short time scales, both in response to direct physical forcing such as buoyancy-driven accumulation in the surface microlayer and wind-driven mixing features such as Langmuir circulations [Azetsu-Scott and Passow, 2004; Wurl *et al.*, 2011], and in response to non-linear biogeochemical forcing. Across-transect CVs for TEP were generally larger than for small-sized chlorophyll and NCP, and often similar in magnitude to large-sized chlorophyll (supporting information, Figure S9). This suggests that even when there is no explicit link between TEP and large-sized chlorophyll or  $^{234}\text{Th}$ , its spatial variability is similar, suggesting control by similarly scaled physical and ecosystem processes.

physical gradients, which might have introduced variability, but probably not a bias in export:NCP given that we sampled across both attracting and repelling FTLE surfaces. Third, it is possible that localized upwelling could inject low-O<sub>2</sub> water (along with productivity-fueling nutrients) into the euphotic zone. While recent observations of R. H. R. Stanley and D. McGillicuddy (manuscript in review, 2015) suggest that the NCP response to such upwelling events is often strong enough to rapidly mask any residual, upwelled O<sub>2</sub> debt in the mixed layer, it is nonetheless possible that the calculated NCP from the O<sub>2</sub>/Ar method is an underestimate of the true NCP value, and that the export:NCP relationship is thus biased high. Finally, the export:NCP relationship could be biased low because NCP includes the production of DOC, which does not contribute to the <sup>234</sup>Th deficit proxy. *Hansell and Carlson* [2001] estimated that annual DOC export was about 15–41% of NCP at BATS. While there are potentially both positive (DOC) and negative (upwelled O<sub>2</sub> debt) biases in NCP, our averaged, high-resolution observations of particle export and NCP agree well enough to suggest that our observations successfully captured highly spatially variable components of export, such as horizontal advection and active zooplankton transport [*Brix et al.*, 2006; *Emerson*, 2014].

## 5. Conclusion

It is likely that upper ocean disequilibria, between NCP and EP, as well as many other fluxes, may be the rule and not the exception. For instance, in a NCP time series at Station ALOHA, *Karl et al.* [2003] observed sporadic episodes of net autotrophy that were required in order to balance observed export, which would have been missed without continuous, high-temporal resolution measurements. Similarly, *Buesseler et al.* [2009] found at ALOHA and in the NW Pacific that spatial variability in <sup>234</sup>Th-derived EP (which does not integrate spatially) was much greater than EP in traps (which do integrate spatially), while both export estimates were more spatially variable than NPP. Several modeling studies conducted to date also suggest the vertical and horizontal decoupling of NCP and export over short spatiotemporal scales. Our snapshot observations show that the two fluxes are indeed horizontally decoupled within 30–40 km transects across regions of strong physical gradients in the subtropical Atlantic. However, as we have hypothesized (Figure 1), these submesoscale features evolve over time scales of days to a few weeks. We also have observed that fluxes likely to be driven by lower trophic-level processes (i.e., NCP) are spatiotemporally decoupled from much higher-variability fluxes driven by higher trophic-level processes (EP). Thus, it will be difficult to decipher the controls of ecosystem processes on export through periodic reoccupations of a single spatial point, while high-spatial resolution measurements at discrete time points (e.g., this study) will not be sufficient to fully characterize of the ocean's biogeochemical and carbon flux balances.

In order to correctly describe the carbon mass balance and biogeochemical processes associated with a submesoscale feature, high resolution, repeated sampling will be necessary. Closure of carbon budgets in the western Sargasso and other similar systems will require future sampling strategies that take into account the very high spatial variability in particulate carbon export and the physical and biological processes that modulate it. Data sets collected over appropriate spatiotemporal sampling scales are also important for comparing rate observations from different locations and times, and for development and validation of numerical models of biogeochemical rate processes. Future efforts must assess the proper spatial and time scales over which biogeochemical rate determinations need to be aggregated, in order to provide robust estimates of mean conditions.

## References

- Abraham, E. R. (1998), The generation of plankton patchiness by turbulent stirring, *Nature*, 391(6667), 577–580.
- Abraham, E. R., C. S. Law, P. W. Boyd, S. J. Lavender, M. T. Maldonado, and A. R. Bowie (2000), Importance of stirring in the development of an iron-fertilized phytoplankton bloom, *Nature*, 407(6805), 727–730.
- Alkire, M. B., et al. (2012), Estimates of net community production and export using high-resolution, Lagrangian measurements of O<sub>2</sub>, NO<sub>3</sub><sup>-</sup>, and POC through the evolution of a spring diatom bloom in the North Atlantic, *Deep Sea Res., Part I*, 64, 157–174, doi:10.1016/j.dsr.2012.01.012.
- Azetsu-Scott, K., and U. Passow (2004), Ascending marine particles: Significance of transparent exopolymer particles (TEP) in the upper ocean, *Limnol. Oceanogr.*, 49(3), 741–748.
- Barkan, E., and B. Luz (2003), High-precision measurements of <sup>17</sup>O/<sup>16</sup>O and <sup>18</sup>O/<sup>16</sup>O of O<sub>2</sub> and O<sub>2</sub>/Ar ratio in air, *Rapid Commun. Mass Spectrom.*, 17(24), 2809–2814, doi:10.1002/rcm.1267.
- Brix, H., N. Gruber, D. M. Karl, and N. R. Bates (2006), On the relationships between primary, net community, and export production in subtropical gyres, *Deep Sea Res., Part II*, 53(5–7), 698–717, doi:10.1016/j.dsr2.2006.01.024.
- Buesseler, K. O., et al. (2006), An assessment of particulate organic carbon to thorium-234 ratios in the ocean and their impact on the application of <sup>234</sup>Th as a POC flux proxy, *Mar. Chem.*, 100, 213–233.

## Acknowledgments

The export and net community production data reported in this paper are available online as part of the accompanying supporting information. All other data are available upon request from the corresponding author (mestapa@skidmore.edu). This study was funded by a NASA Ocean Carbon and Biogeochemistry program grant (NNX11AL94G). M.L.E. was supported by a WHOI Postdoctoral Scholar fellowship. R.S. was supported by a NASA ACE grant (NNX12AJ25G). Ship time was funded by an NSF grant to the BATS program (OCE-0752366). Satellite altimeter products were produced by Ssalto/Duacs and distributed by Aviso, with support from CNES (<http://www.aviso.oceanobs.com/duacs/>). Many people contributed to the intensive sampling and analytical efforts in this study, and their efforts are greatly appreciated: E. Aghassi, S. Allender, E. Black, J. Casey, E. Fields, V. Garçon, S. Goldberg, S. Pike, Z. Sandwith, E. Stassinis, J. Sudre, K. Terpis, and the captain and crew of the R/V *Atlantic Explorer*. This manuscript was greatly improved through the thoughtful comments of Steve Emerson, the Associate Editor, and an anonymous reviewer.

- Buesseler, K. O., S. Pike, K. Maiti, C. H. Lamborg, D. A. Siegel, and T. W. Trull (2009), Thorium-234 as a tracer of spatial, temporal and vertical variability in particle flux in the North Pacific, *Deep Sea Res., Part I*, 56, 1143–1167, doi:10.1016/j.dsr.2009.04.001.
- Callil, P. H. R., and K. J. Richards (2010), Transient upwelling hot spots in the oligotrophic North Pacific, *J. Geophys. Res.*, 115, C02003, doi:10.1029/2009JC005360.
- Cassar, N., B. A. Barnett, M. L. Bender, J. Kaiser, R. C. Hamme, and B. Tilbrook (2009), Continuous high-frequency dissolved O<sub>2</sub>/Ar measurements by equilibrator inlet mass spectrometry, *Anal. Chem.*, 81(5), 1855–1864, doi:10.1021/ac802300u.
- Coale, K. H., and K. W. Bruland (1987), Oceanic stratified euphotic zone as elucidated by <sup>234</sup>Th: <sup>238</sup>U disequilibria, *Limnol. Oceanogr.*, 32(1), 189–200.
- d'Ovidio, F., V. Fernández, E. Hernández-García, and C. López (2004), Mixing structures in the Mediterranean Sea from finite-size Lyapunov exponents, *Geophys. Res. Lett.*, 31, L17203, doi:10.1029/2004GL020328.
- d'Ovidio, F., S. De Monte, S. Alvain, Y. Dandonneau, and M. Lévy (2010), Fluid dynamical niches of phytoplankton types, *Proc. Natl. Acad. Sci. U.S.A.*, 107(43), 18,366–18,370.
- Denman, K. L., and T. Platt (1976), Variance spectrum of phytoplankton in a turbulent ocean, *J. Mar. Res.*, 34(4), 593–601.
- Durand, M. D., and R. J. Olson (1996), Contributions of phytoplankton light scattering and cell concentration changes to diel variations in beam attenuation in the equatorial Pacific from flow cytometric measurements of pico-, ultra- and nanoplankton, *Deep Sea Res., Part II*, 43(4–6), 891–906, doi:10.1016/0967-0645(96)00020-3.
- Emerson, S. (2014), Annual net community production and the biological carbon flux in the ocean: Ocean biological organic carbon flux, *Global Biogeochem. Cycles*, 28, 14–28, doi:10.1002/2013GB004680.
- Engel, A. (2009), Determination of marine gel particles, in *Practical Guidelines for the Analysis of Seawater*, edited by O. Wurl, pp. 125–142, CRC Press, Boca Raton, Fla.
- Falkowski, P. G., R. T. Barber, and V. Smetacek (1998), Biogeochemical controls and feedbacks on ocean primary production, *Science*, 281(5374), 200–206, doi:10.1126/science.281.5374.200.
- Fawcett, S. E., M. W. Lomas, B. B. Ward, and D. M. Sigman (2014), The counterintuitive effect of summer-to-fall mixed layer deepening on eukaryotic new production in the Sargasso Sea: Seasonal  $\delta^{15}\text{N}$  of phytoplankton at BATS, *Global Biogeochem. Cycles*, 28, 86–102, doi:10.1002/2013GB004579.
- Garçon, V. C., A. Oschlies, S. C. Doney, D. McGillicuddy, and J. Waniek (2001), The role of mesoscale variability on plankton dynamics in the North Atlantic, *Deep Sea Res., Part II*, 48(10), 2199–2226.
- Geider, R. J. (1987), Light and temperature dependence of the carbon to chlorophyll a ratio in microalgae and cyanobacteria: Implications for physiology and growth of phytoplankton, *New Phytol.*, 106(1), 1–34, doi:10.2307/2434683.
- Guidi, L., et al. (2012), Does eddy-eddy interaction control surface phytoplankton distribution and carbon export in the North Pacific Subtropical Gyre?, *J. Geophys. Res.*, 117, G02024, doi:10.1029/2012JG001984.
- Hansell, D. A., and C. A. Carlson (2001), Biogeochemistry of total organic carbon and nitrogen in the Sargasso Sea: Control by convective overturn, *Deep Sea Res., Part II*, 48(8), 1649–1667.
- Harrison, C. S., and G. A. Glatzmaier (2010), Lagrangian coherent structures in the California Current System—Sensitivities and limitations, *Geophys. Astrophys. Fluid Dyn.*, 106(1), 22–44, doi:10.1080/03091929.2010.532793.
- Harrison, C., D. Siegel, and S. Mitarai (2013), Filamentation and eddy – eddy interactions in marine larval accumulation and transport, *Mar. Ecol. Prog. Ser.*, 472, 27–44, doi:10.3354/meps10061.
- Ho, D. T., C. S. Law, M. J. Smith, P. Schlosser, M. Harvey, and P. Hill (2006), Measurements of air-sea gas exchange at high wind speeds in the Southern Ocean: Implications for global parameterizations, *Geophys. Res. Lett.*, 33, L16611, doi:10.1029/2006GL026817.
- Hooker, S. B., et al. (2005), The second SeaWiFS HPLC analysis round-robin experiment (SeaHARRE-2), Tech. Memo., Goddard Space Flight Center, Greenbelt, Md.
- Hosoda, S., T. Ohira, K. Sato, and T. Suga (2010), Improved description of global mixed-layer depth using Argo profiling floats, *J. Oceanogr.*, 66(6), 773–787.
- Kalnay, E., et al. (1996), The NCEP/NCAR 40-year reanalysis project, *Bull. Am. Meteorol. Soc.*, 77(3), 437–471, doi:10.1175/1520-0477(1996)077<0437:TNYRP>2.0.CO;2.
- Karl, D. M., E. A. Laws, P. Morris, P. J. leB. Williams, and S. Emerson (2003), Global carbon cycle (communication arising): Metabolic balance of the open sea, *Nature*, 426(6962), 32–32, doi:10.1038/426032a.
- Laws, E. A. (1991), Photosynthetic quotients, new production and net community production in the open ocean, *Deep Sea Res., Part A*, 38(1), 143–167.
- Levy, M., and A. P. Martin (2013), The influence of mesoscale and submesoscale heterogeneity on ocean biogeochemical reactions, *Global Biogeochem. Cycles*, 27, 1139–1150, doi:10.1002/2012GB004518.
- Lévy, M., R. Ferrari, P. J. S. Franks, A. P. Martin, and P. Rivière (2012), Bringing physics to life at the submesoscale, *Geophys. Res. Lett.*, 39, L14602, doi:10.1029/2012GL052756.
- Lomas, M. W., D. K. Steinberg, T. Dickey, C. A. Carlson, N. B. Nelson, R. H. Condon, and N. R. Bates (2010), Increased ocean carbon export in the Sargasso Sea linked to climate variability is countered by its enhanced mesopelagic attenuation, *Biogeosciences*, 7(1), 57–70.
- Lomas, M. W., N. R. Bates, R. J. Johnson, A. H. Knap, D. K. Steinberg, and C. A. Carlson (2013), Two decades and counting: 24-years of sustained open ocean biogeochemical measurements in the Sargasso Sea, *Deep Sea Res., Part II*, 93, 16–32, doi:10.1016/j.dsr2.2013.01.008.
- Luz, B., and E. Barkan (2009), Net and gross oxygen production from O<sub>2</sub>/Ar, <sup>17</sup>O/<sup>16</sup>O and <sup>18</sup>O/<sup>16</sup>O ratios, *Aquat. Microb. Ecol.*, 56, 133–145, doi:10.3354/ame01296.
- Mackas, D. L., and C. M. Boyd (1979), Spectral analysis of zooplankton spatial heterogeneity, *Science*, 204(4388), 62–64, doi:10.2307/1747974.
- Marra, J. F., V. P. Lance, R. D. Vaillancourt, and B. R. Hargreaves (2014), Resolving the ocean's euphotic zone, *Deep Sea Res., Part I*, 83, 45–50, doi:10.1016/j.dsr.2013.09.005.
- Martin, A. P. (2003), Phytoplankton patchiness: The role of lateral stirring and mixing, *Progress Oceanogr.*, 57(2), 125–174, doi:10.1016/S0079-6611(03)00085-5.
- Martin, P., R. S. Lampitt, M. Jane Perry, R. Sanders, C. Lee, and E. D'Asaro (2011), Export and mesopelagic particle flux during a North Atlantic spring diatom bloom, *Deep Sea Res., Part I*, 58(4), 338–349, doi:10.1016/j.dsr.2011.01.006.
- Martin, P., et al. (2013), Iron fertilization enhanced net community production but not downward particle flux during the Southern Ocean iron fertilization experiment LOHAFEX: NCP and particle flux during LOHAFEX, *Global Biogeochem. Cycles*, 27, 871–881, doi:10.1002/gbc.20077.
- Nencioli, F., F. d'Ovidio, A. M. Doglioli, and A. A. Petrenko (2011), Surface coastal circulation patterns by in-situ detection of Lagrangian coherent structures: In-situ detection of coastal LCS, *Geophys. Res. Lett.*, 38, L17604, doi:10.1029/2011GL048815.

- Nightingale, P. D., G. Malin, C. S. Law, A. J. Watson, P. S. Liss, M. I. Liddicoat, J. Boutin, and R. C. Upstill-Goddard (2000), In situ evaluation of air-sea gas exchange parameterizations using novel conservative and volatile tracers, *Global Biogeochem. Cycles*, *14*(1), 373–387.
- Owens, S. A. (2012), Advances in measurements of particle cycling and fluxes in the ocean, PhD thesis, Massachusetts Institute of Technology and the Woods Hole Oceanographic Institution, Woods Hole, Mass.
- Owens, S. A., K. O. Buesseler, and K. W. W. Sims (2011), Re-evaluating the  $^{238}\text{U}$ -salinity relationship in seawater: Implications for the  $^{238}\text{U}$ - $^{234}\text{Th}$  disequilibrium method, *Mar. Chem.*, *127*(1–4), 31–39, doi:10.1016/j.marchem.2011.07.005.
- Owens, S. A., K. O. Buesseler, and S. Pike (2015), Thorium-234 as a tracer of particle dynamics and upper ocean export in the Atlantic Ocean, *Deep Sea Res., Part II*, *116*, 42–59, doi:10.1016/j.dsr2.2014.11.010.
- Passow, U. (2001), Origin of transparent exopolymer particles (TEP) and their role in the sedimentation of particulate matter, *Cont. Shelf Res.*, *21*, 327–346.
- Passow, U., J. Dunne, J. W. Murray, L. Balistrieri, and A. L. Alldredge (2006), Organic carbon to  $^{234}\text{Th}$  ratios of marine organic matter, *Mar. Chem.*, *100*(3–4), 323–336, doi:10.1016/j.marchem.2005.10.020.
- Pike, S. M., K. O. Buesseler, J. Andrews, and N. Savoye (2005), Quantification of  $^{234}\text{Th}$  recovery in small volume sea water samples by inductively coupled plasma-mass spectrometry, *J. Radioanal. Nucl. Chem.*, *263*(2), 355–360.
- Quigley, M. S., P. H. Santschi, C.-C. Hung, L. Guo, and B. D. Honeyman (2002), Importance of acid polysaccharides for  $^{234}\text{Th}$  complexation to marine organic matter, *Limnol. Oceanogr.*, *47*(2), 367–377, doi:10.2307/3068983.
- Resplandy, L., A. P. Martin, F. Le Moigne, P. Martin, A. Aquilina, L. Mémerly, M. Lévy, and R. Sanders (2012), How does dynamical spatial variability impact  $^{234}\text{Th}$ -derived estimates of organic export?, *Deep Sea Res., Part I*, *68*, 24–45, doi:10.1016/j.dsr.2012.05.015.
- Reuer, M. K., B. A. Barnett, M. L. Bender, P. G. Falkowski, and M. B. Hendricks (2007), New estimates of Southern Ocean biological production rates from  $\text{O}_2/\text{Ar}$  ratios and the triple isotope composition of  $\text{O}_2$ , *Deep Sea Res., Part I*, *54*(6), 951–974, doi:10.1016/j.dsr.2007.02.007.
- Richerson, P., R. Armstrong, and C. R. Goldman (1970), Contemporaneous disequilibrium, a new hypothesis to explain the “paradox of the plankton”, *Proc. Natl. Acad. Sci. U.S.A.*, *67*(4), 1710–1714.
- Samelson, R. M. (2013), Lagrangian motion, coherent structures, and lines of persistent material strain, *Annu. Rev. Mar. Sci.*, *5*(1), 137–163, doi:10.1146/annurev-marine-120710-100819.
- Shadden, S. C., F. Lekien, J. D. Paduan, F. P. Chavez, and J. E. Marsden (2009), The correlation between surface drifters and coherent structures based on high-frequency radar data in Monterey Bay, *Deep Sea Res., Part II*, *56*(3–5), 161–172, doi:10.1016/j.dsr2.2008.08.008.
- Siegel, D. A., et al. (2001), Bio-optical modeling of primary production on regional scales: The Bermuda BioOptics project, *Deep Sea Res., Part II*, *48*(8), 1865–1896.
- Sieracki, M. E., P. G. Verity, and D. K. Stoecker (1993), Plankton community response to sequential silicate and nitrate depletion during the 1989 North Atlantic spring bloom, *Deep Sea Res., Part II*, *40*(1–2), 213–225, doi:10.1016/0967-0645(93)90014-E.
- Stanley, R. H. R., W. J. Jenkins, D. E. Lott, and S. C. Doney (2009), Noble gas constraints on air-sea gas exchange and bubble fluxes, *J. Geophys. Res.*, *114*, C11020, doi:10.1029/2009JC005396.
- Stanley, R. H. R., J. B. Kirkpatrick, N. Cassar, B. A. Barnett, and M. L. Bender (2010), Net community production and gross primary production rates in the western equatorial Pacific: Western equatorial Pacific production, *Global Biogeochem. Cycles*, *24*, GB4001, doi:10.1029/2009GB003651.
- Strickland, J. D. H., and T. R. Parsons (1972), *A Practical Handbook of Seawater Analysis*, Fisheries Research Board of Canada.
- Turnewitsch, R., J.-L. Reyss, J. Nycander, J. J. Waniek, and R. S. Lampitt (2008), Internal tides and sediment dynamics in the deep sea—Evidence from radioactive  $^{234}\text{Th}$ / $^{238}\text{U}$  disequilibria, *Deep Sea Res., Part I*, *55*(12), 1727–1747, doi:10.1016/j.dsr.2008.07.008.
- Volk, T., and M. I. Hoffert (1985), Ocean carbon pumps: Analysis of relative strengths and efficiencies in ocean-driven atmospheric  $\text{CO}_2$  changes, in *The Carbon Cycle and Atmospheric  $\text{CO}_2$ : Natural Variations Archaean to Present*, pp. 99–110, AGU, Washington, D. C.
- Wanninkhof, R. (1992), Relationship between wind speed and gas exchange over the ocean, *J. Geophys. Res.*, *97*(C5), 7373–7382.
- Welschmeyer, N. A. (1994), Fluorometric analysis of chlorophyll a in the presence of chlorophyll b and pheopigments, *Limnol. Oceanogr.*, *39*(8), 1985–1992.
- Wurl, O., L. Miller, and S. Vagle (2011), Production and fate of transparent exopolymer particles in the ocean, *J. Geophys. Res.*, *116*, C00H13, doi:10.1029/2011JC007342.